Structural integration of a full-composite, double-walled, vacuum-insulated, cryo-compressed tank for the Flying V: a numerical study

Poorte, V.K.; Bergsma, O.K.; van Campen, J.M.J.F.; Alderliesten, R.C.

DOI
10.2514/6.2024-0834

Publication date
2024

Document Version
Final published version

Published in
Proceedings of the AIAA SCITECH 2024 Forum

AIAA SciTech Forum
8-12 January 2024, Orlando, FL
AIAA SCITECH 2024 Forum

10.2514/6.2024-0834

Structural integration of a full-composite, double-walled, vacuum-insulated, cryo-compressed hydrogen tank.

Victor K. Poorte*, Otto K. Bergsma, Julien M.J.F. van Campen, and Renè C. Alderliesten
Faculty of Aerospace Engineering, Delft University of Technology, 2629 HS Delft, The Netherlands

Hydrogen is being investigated as aviation fuel, with the objective to achieve an energy transition for the aviation sector. Effective storage solutions are crucial to mitigate the aerodynamic penalty caused by its low volumetric energy density. The focus of this study is the integration of a cryo-compressed vacuum-insulated storage vessel into the primary structure of aircraft, aiming to enhance structural efficiency. This is achieved by implementing analytical methods to analyse the thermo-mechanical loading of the inner and outer walls of the fuel tank. It is envisioned that the inner wall rather than the outer wall is more suitable to sustain additional loads. However, it is unclear how the cryogenic environment affects the stress state of the composite material. This research contributes to the development of hydrogen-powered aircraft by addressing critical aspects of hydrogen storage, thereby driving the energy transition within the aviation industry.

Nomenclature

Greek symbols

α_i	=	Thermal expansion coefficient, with $i = x, y, z, \theta,$ and r; or material property, with $i = 1, 2$
β	=	Material properties derived variable
Δ	=	Variation
η	=	Thermal stress developed in material
γ_i	=	Shear strain, with $i = 0, z, \theta,$ r
ν_{ij}	=	Poisson ratio, with $i, j = x, y, z$
ϕ	=	Winding angle
σ	=	Stress
τ	=	Shear stress
θ	=	Angular coordinate
ε_i	=	Strain, with $i = x, y, z, \theta, r,$ and 0
ξ	=	Material properties derived variable

Latin symbols

$\bar{C}_{ij}$	=	Material compliance in global coordinate system, with $i = 1, 2, 3, 4, 5, 6$; or geometric property for buckling
$\bar{D}_{ij}$	=	Geometric property for buckling, with $i = x, y$
$\bar{E}_{ij}$	=	Geometric property for buckling, with $i = x, y$
$\bar{G}_{xy}$	=	Geometric property for buckling
$\bar{K}_{xy}$	=	Geometric property for buckling
$\mathbf{a}$	=	Solution vector for the displacement fields
$\mathbf{f}_{ext}$	=	External loading vector
$\mathbf{K}$	=	Internal stiffness matrix
$\mathbf{K}_{sys}$	=	System stiffness matrix
$\mathbf{r}$	=	Force residual
$A^{(k)}$	=	Shear stress integration constant for the k^{th} layer; or material properties rotation matrix of layer k
A_{ij}	=	Buckling load matrix entries, with $i, j = 1, 2, 3$; or laminate A matrix entries, with $i, j = 1, 2, 3$
$B^{(k)}$	=	Shear stress integration constant for the k^{th} layer
B_{ij}	=	Laminate B matrix entries, with $i, j = 1, 2, 3$

*Contact: V.K.Poorte@tudelft.nl.

C_{ij} = Material compliance in material's coordinate system, with $i, j = x, y, z$
$D^{(k)}$ = Displacement field unknown for the k^{th} layer
D_{ij} = Laminate D matrix entries, with $i, j = 1, 2, 3$
$d_i^{(k)}$ = Displacement continuity entry for the k^{th} layer, with $i = 1, 2, e, l, t$
$E^{(k)}$ = Displacement field unknown for the k^{th} layer
E_i = Elastic modulus, with $i = x, y, z$
$e_i^{(k)}$ = Elongation boundary condition entry for the k^{th} layer, with $i = 1, 2, e, l, t$
F_a = Axial load
g = Boundary condition
G_{ij} = Shear modulus, with $i = x, y, z$
k = Laminate layer index
L = Cylinder length
m, n = Rotational cosine and sine; or number of buckling half waves
N_x = Distributed buckling load
p = Pressure
r = Radius, or radial coordinate
R_i = Critical buckling ratio, with $i = p, c$
$s_i^{(k)}$ = Stress continuity entry for the k^{th} layer, with $i = 1, 2, e, l, t$
T = Temperature
$t_i^{(k)}$ = Twist boundary condition entry for the k^{th} layer, with $i = 1, 2, e, l, t$
u = Displacement field
X^C = Ultimate compressive failure strength longitudinal direction
X^T = Ultimate in-plane shear strength
X^T = Ultimate tensile failure strength longitudinal direction
Y^C = Ultimate compressive failure strength traverse direction
Y^T = Ultimate tensile failure strength traverse direction
z = Longitudinal coordinate

Subscripts

0 = Initial
c = Compression
cr = Critical
e = Extension
i = Inner; or layer index
l = Load
o = Outer
p = Pressure
t = Twist

I. Introduction

In support of the Paris Agreement, the aviation industry has set its target to achieve net-zero carbon emissions by the year 2050. This is to be achieved by increased efficiency, a transition in energy sources, and innovation across the entire sector. A lot can be achieved with efficiency gains, but a fundamental shift can be achieved by transitioning to a new energy source. Different sources are the subject of study: sustainable aviation fuels (SAF), battery power or hydrogen fuel. All solutions naturally have their advantages, but come with the inevitable drawbacks. This research focuses on hydrogen fuel.

Hydrogen is a suitable energy carrier considering its gravimetric energy density, with a value that lies around 120 MJ/kg. This leads to a three times higher energy density compared to jet fuel, which has a value of 43 MJ/kg. The volumetric energy density of hydrogen is one of the drawbacks withholding implementation. Assuming a density of 70 kg/m^3, it has a volumetric energy density of 8 MJ/m^3, which is four times lower than that of traditional aviation fuels, which has an energy density of 35 MJ/m^3. The increase in required volume inevitably has consequences on the aerodynamic performance of the aircraft.

The assumed density of 70 kg/m^3 can be achieved by liquefying the fuel or by storing it in the cryo-compressed state. To achieve the liquid state hydrogen needs to be cooled below 33 K at a pressure of 12.8 bar, where further cooling is required to achieve lower pressure values. In the cryo-compressed state, the temperature ranges between 33-100 K, and the pressure is between 300-1000 bar. A key challenge for the fuel transition is to design a vessel which can house the fuel in the defined conditions in an efficient and safe manner.

In this study, a double-walled vacuum-insulated storage vessel which holds the hydrogen in the cryo-compressed state is investigated. The structure is thus required to operate at high-pressure values while maintaining the hydrogen in the prescribed temperature range. Given the high gravimetric efficiency that can be achieved with composite pressure vessels, it is chosen to investigate this type of storage. Furthermore, the fuel tank requires insulation to limit the heat flow into the system, to maintain the prescribed temperature range and limit pressure rise in the tank. For this foam type of insulation and vacuum insulation are commonly suggested [1]. In this study, the vacuum-insulated solution is investigated. In Figure 1 an example of a double-walled vacuum-insulated storage vessel is reported. Figure 1 also depicts the connection between the inner and outer shells, these are crucial to keeping the inner shell in place. One of the design challenges of the connectors is that they need to limit thermal conduction.

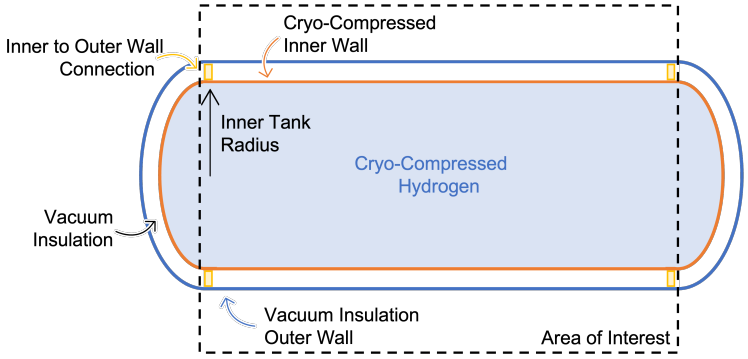

Fig. 1 Example of a double-walled vacuum insulated storage vessel.

A high degree of integration commonly leads to a lighter structure, which increases the aircraft's efficiency, leading to a positive snowball effect. Currently, the wing box of the aircraft also serves as the fuel tank. In a similar fashion, the degree of integration of the hydrogen fuel system can be increased by making it part of the primary structure. To achieve this, the physical shells need to carry additional load cases besides the thermo-mechanical loading required to store the hydrogen or maintain the vacuum. TFigure 1 shows that only the body section of the tank is considered, as this part of the structure is assumed to carry the additional loads. It is unclear whether the load path should go through the inner or outer wall, given the different original requirements of the structure. This work aims at developing and implementing a method which enables the analysis of composite shells subjected to thermo-mechanical loading. With the developed methods it shall be analysed which of the two shells is more suited to carry additional loads.

II. Methods

The study investigates the integrability of an all-composite vacuum-insulated cryo-compressed hydrogen storage vessel into the primary structure of an aircraft. The analysis focuses on the body section of the tank, as this part of the structure is envisioned to bear external loads. Analytical methods are developed to analyze composite cylinders and define the structure's viable design space. When the viable design space is defined, the optimal solution can be pinpointed for the chosen tank dimensions and prescribed load case.

Two failure modes are considered in the current study: material failure and structural instability. Material properties and the selected material failure criterion are reported in subsection II.A. A non-linear analytical method is developed in subsection II.B and subsection II.C, which enables to determination of the stress/strain state of a thick-walled composite cylinder subjected to thermo-mechanical loading. The analytical model is an elaboration on the work of M. Xia et al. [2, 3]. [3] enables the analysis of thermo-mechanically loaded sandwich pipes; however, this analysis is limited to

symmetric laminates. As such, a combination of the two cited works is taken to extend the possibility of analysis of non-symmetric laminates. Furthermore, the boundary conditions are altered to enable axial loading. The developed model is linear. As such it does not account for the change in geometry of the vessel, and as a consequence a change in loading. The model is non-linearised to account for these phenomena, as described in subsection II.C. Structural instability is accounted for by considering shell buckling due to axial loading, and the buckling of the outer shell subjected to vacuum. The models used to account for buckling are reported in subsection II.D. Finally, subsection II.E provides considerations associated with manufacturing.

A. Material

The T300/N5208 material system is used in the current study, with properties reported in Table 1. The out-of-plane properties of the material are assumed to be equal to the traverse properties. Material failure is determined using the Tsai-Wu failure criterion.

Table 1 Properties of T300/N5208 unidirectional lamina [4].

Variable	Symbol	Value	Units
Longitudinal modulus	E_x	181.0	GPa
Traverse modulus	E_y	10.3	GPa
Shear modulus	G_{xy}	7.17	GPa
Major Poisson ratio	ν_{xy}	0.28	-
Longitudinal thermal expansion coefficient	α_x	0.02	10^{-6}/K
Traverse thermal expansion coefficient	α_y	22.5	10^{-6}/K
Ultimate tensile strength longitudinal direction	X^T	1500	MPa
Ultimate compressive strength longitudinal direction	X^C	1500	MPa
Ultimate tensile strength traverse direction	Y^T	40	MPa
Ultimate compressive strength traverse direction	Y^C	146	MPa
Ultimate in-plane shear strength	S	68	MPa

B. Analytical Thick Walled Pressure Vessel Model

The objective of the analytical model is to determine the layers' strains, such that these can be used in combination with the Tsai-Wu failure criterion to establish whether the design can withstand the loads.

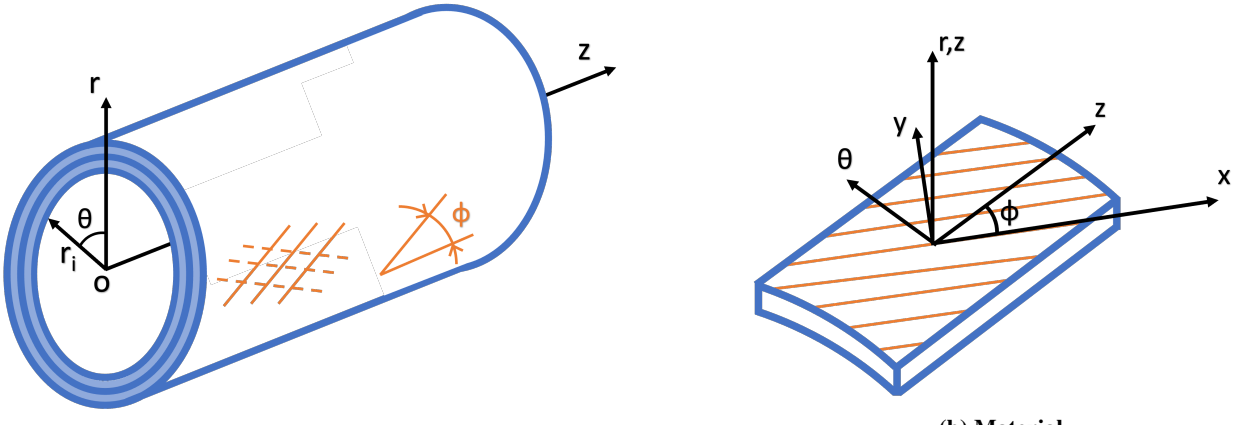

(a) Vessel **(b) Material**

Fig. 2 Vessel radial coordinate system (a) and material coordinate system (b).

The steps performed to obtain the strains of the system are equal to the ones performed by Xia et al. [2, 3], the reader is thus referred to the cited work for a more detailed description. The difference with respect to the cited work lies in the assumed deformation fields. These account for the thermal loading and twist of the vessel. The assumed displacement field is reported in Equation 1. See Figure 2 as a reference for the selected coordinate system. In the displacement field, α_1 and α_2 are as defined in Equation 2. The displacement is a function of the off-axis material parameters, denoted with the $\bar{C}_{ij}$ terms, the radial location r in the tube, the β term, which is equal to $\sqrt{\bar{C}_{22}^{(k)}/\bar{C}_{33}^{(k)}}$, the material thermal property $\eta^{(k)}$, which is equal to $(\xi_r^{(k)} - \xi_\theta^{(k)})/\bar{C}_{11}^{(k)}$, where $\xi_r^{(k)}$ and $\xi_\theta^{(k)}$ are the thermal stress contributions as defined in Equation 3. Finally, $D^{(k)}$, $E^{(k)}$, ε_0, and γ_0 are unknowns which are to be determined using the boundary conditions of the system. $D^{(k)}$ and $E^{(k)}$ are non-physical parameters which scale the radius exponents to match the displacement. ε_0 and γ_0 are the constant axial strain and twist.

$$u_r^{(k)} = D^{(k)} r^{\beta^{(k)}} + E^{(k)} r^{-\beta^{(k)}} + \alpha_1^{(k)} \varepsilon_0 r + \alpha_2^{(k)} \gamma_0 r^2 + \frac{\eta^{(k)} \Delta T}{1 - \left(\beta^{(k)}\right)^2}, \quad \text{for} \quad \beta \neq 0 \tag{1a}$$

$$u_r^{(k)} = D^{(k)} r + E^{(k)}/r + \frac{\alpha_3}{2} \varepsilon_0 r \ln r + \alpha_2^{(k)} \gamma_0 r^2 + \frac{\eta^{(k)} \Delta T}{2} r \ln r, \quad \text{for} \quad \beta = 1 \tag{1b}$$

$$\alpha_1 = \frac{\bar{C}_{12}^{(k)} - \bar{C}_{13}^{(k)}}{\bar{C}_{33}^{(k)} - \bar{C}_{22}^{(k)}} \quad \text{and} \quad \alpha_2 = \frac{\bar{C}_{26}^{(k)} - 2\bar{C}_{36}^{(k)}}{4\bar{C}_{33}^{(k)} - \bar{C}_{22}^{(k)}} \tag{2}$$

$$\begin{aligned} \xi_r^{(k)} &= \bar{C}_{11}^{(k)} \alpha_z^{(k)} + \bar{C}_{12}^{(k)} \alpha_\theta^{(k)} + \bar{C}_{13}^{(k)} \alpha_3^{(k)} \\ \xi_\theta^{(k)} &= \bar{C}_{12}^{(k)} \alpha_z^{(k)} + \bar{C}_{22}^{(k)} \alpha_\theta^{(k)} + \bar{C}_{23}^{(k)} \alpha_3^{(k)} \end{aligned} \tag{3}$$

$$\alpha_3 = \frac{\bar{C}_{12}^{(k)} - \bar{C}_{13}^{(k)}}{\bar{C}_{33}^{(k)}} \tag{4}$$

When $D^{(k)}$, $E^{(k)}$, ε_0, and γ_0 are determined, the strains of each layer can be computed. 2·N + 2 unknowns are left undetermined, where N represents the number of layers. A system of equations is set up based on the boundary conditions of the cylinder, displacement continuity, and stress continuity. The boundary conditions are equal to the ones reported in [2, 3], with the exception of the axial equilibrium boundary condition, where the axial load (F_a) is added, as reported in Equation 26.

$$2\pi \sum_{k=1}^{n} \int_{r_{k-1}}^{r_k} \sigma_r^{(k)} r \mathrm{d}r = \pi r_i^2 (p_i - p_o) + F_a \tag{5}$$

With the provided boundary conditions, the system of equations can be set up to determine the unknowns $D^{(k)}$, $E^{(k)}$, ε_0, and γ_0. An example for a four-layer cylinder is reported in Equation 6. The first three rows in the matrix represent the displacement continuity condition between the layers. The fourth to eighth layers present the stress continuity of the layers, where the fourth and eighth rows originate from the traction condition at the inner and outer surfaces, respectively, while the remaining four stem from stress continuity at the layer interfaces. The penultimate row captures the axial elongation boundary, while the last row emanates from the twist boundary condition.

$$
\begin{bmatrix}
d_1^{(1)} & -d_1^{(2)} & 0 & 0 & d_2^{(1)} & -d_2^{(2)} & 0 & 0 & d_e^{(1)} - d_e^{(2)} & d_t^{(1)} - d_t^{(2)} \\
0 & d_1^{(2)} & -d_1^{(3)} & 0 & 0 & d_2^{(2)} & -d_2^{(3)} & 0 & d_e^{(2)} - d_e^{(3)} & d_t^{(2)} - d_t^{(3)} \\
0 & 0 & d_1^{(3)} & -d_1^{(4)} & 0 & 0 & d_2^{(3)} & -d_2^{(4)} & d_e^{(3)} - d_e^{(4)} & d_t^{(3)} - d_t^{(4)} \\
s_1^{(1)} & 0 & 0 & 0 & s_2^{(1)} & 0 & 0 & 0 & s_e^{(1)} & s_t^{(1)} \\
s_1^{(1)} & -s_1^{(2)} & 0 & 0 & s_2^{(1)} & -s_2^{(2)} & 0 & 0 & s_e^{(1)} - s_e^{(2)} & s_t^{(1)} - s_t^{(2)} \\
0 & s_1^{(1)} & -s_1^{(2)} & 0 & 0 & s_2^{(1)} & -s_2^{(2)} & 0 & s_e^{(2)} - s_e^{(3)} & s_t^{(2)} - s_t^{(3)} \\
0 & 0 & s_1^{(1)} & -s_1^{(2)} & 0 & 0 & s_2^{(1)} & -s_2^{(2)} & s_e^{(3)} - s_e^{(4)} & s_t^{(3)} - s_t^{(4)} \\
0 & 0 & 0 & s_1^{(4)} & 0 & 0 & 0 & s_2^{(4)} & s_e^{(4)} & s_t^{(4)} \\
e_1^{(1)} & e_1^{(2)} & e_1^{(4)} & e_1^{(4)} & e_2^{(1)} & e_2^{(2)} & e_2^{(3)} & e_2^{(4)} & e_e & e_t \\
t_1^{(1)} & t_1^{(2)} & t_1^{(4)} & t_1^{(4)} & t_2^{(1)} & t_2^{(2)} & t_2^{(3)} & t_2^{(4)} & t_e & t_t
\end{bmatrix}
\begin{Bmatrix}
D^{(1)} \\ D^{(2)} \\ D^{(3)} \\ D^{(4)} \\ E^{(1)} \\ E^{(2)} \\ E^{(3)} \\ E^{(4)} \\ \varepsilon_0 \\ \gamma_0
\end{Bmatrix} =
\begin{Bmatrix}
\left(d_l^{(2)} - d_l^{(1)}\right)\Delta T \\
\left(d_l^{(3)} - d_l^{(2)}\right)\Delta T \\
\left(d_l^{(4)} - d_l^{(3)}\right)\Delta T \\
-p_i - s_l^{(1)}\Delta T \\
\left(s_l^{(2)} - s_l^{(1)}\right)\Delta T \\
\left(s_l^{(3)} - s_l^{(2)}\right)\Delta T \\
\left(s_l^{(4)} - s_l^{(3)}\right)\Delta T \\
s_l^{(4)}\Delta T - p_0 \\
\frac{(p_i - p_0)r_i^2}{2} + \frac{F_a}{2\pi} + \frac{\Delta T}{2}\sum_{k=1}^{4} e_l^{(k)} \\
\Delta T \sum_{k=1}^{4} t_l^{(k)}
\end{Bmatrix} \tag{6}
$$

The entries for the system of equations are reported in the Appendix. The displacement entries for the matrix are computed using the relations in Equation 24, the stress entries are computed using the relations reported in Equation 25, the entries for the axial elongations can be computed with the relations reported in Equation 26, while the entries associated with axial twist are reported in Equation 27. Finally, the load vector entries are reported in Equation 28. The assumed deformation field with *beta* value of one has some altered entries for the system of equations. The entries for the matrix are reported in Equation 29, whereas the terms for the load vector are as shown Equation 28.

The system of equations can also be written in the format as presented in Equation 7, where the constructed matrix can be considered as a stiffness matrix, **a** is the solution vector, and $\mathbf{f}_{ext}$ is the loading vector. This format is later used in the non-linearisation of the analytical model.

$$\mathbf{f}_{ext} = \mathbf{K}\mathbf{a} \tag{7}$$

The analytical model has been compared to literature [2–4] and a simplified finite element model, and has been found to show good correlation. Literature provides a basis to verify the model with respect to previously derived models. Finite element model verification is done to verify the additional properties of the analytical model, such as the thermal and axial loading of non-symmetric tubes.

C. Analytical Model Non-Linearisation

The analytical model reported in subsection II.B captures linear deformations of a composite cylinder subject to thermo-mechanical loading. In this section, the model is taken and non-linearised. The non-linearities accounted for in this study are the change in the radius of the cylinder, the change in thickness of the cylinder, and the variation in ply angles. As is common in non-linear analysis, the load is applied in time steps, where for each step the system of equations is updated iteratively until the inner and outer loads are in balance. The equilibrium yields a solution vector (**a**) as denoted in Equation 7. In the iterative process, the residual minimisation technique is chosen, with the residual being the difference between the inner and outer loading vectors. The residual is minimised using the full

Newton-Raphson method. This method is chosen as it is effective when the load vector also changes with changing geometry. For example in the case of a pressure vessel, the change in cross-section leads to a change in axial loading.

The inner radius of the vessel at time instance $i+1$ is a function of the original inner radius (r_0) and the global strain in the tangent direction of the inner layer at time step i ($\varepsilon_{\theta,i}$), as depicted in Equation 8.

$$r_{i+1} = r_0 \left(1 + \varepsilon_{\theta,i}\right) \tag{8}$$

The thickness of a layer k at time instance $i+1$ is a function of the original thickness ($t_0^{(k)}$) and strain in the out of plane direction at time step i ($\varepsilon_{r,i}^{(k)}$), as depicted in Equation 9.

$$t_{i+1}^{(k)} = t_0^{(k)} \left(1 + \varepsilon_{r,i}^{(k)}\right) \tag{9}$$

The change in the winding angle of layer k can be obtained with a simple derivation based on the visual aid reported in Figure 3. The derivation to obtain the new fibre angle ($\phi_{i+1}^{(k)}$) is reported in Equation 10 [5, 6]. In the original and deformed state, the tangent of the fibre angle (ϕ) can be given by the ratio between a segment in the traverse direction (b) and longitudinal direction (a). The variation in the segment length is a function of the original segment length and the strain in the corresponding direction. The ratio between the original segments can then be related to the original winding angle.

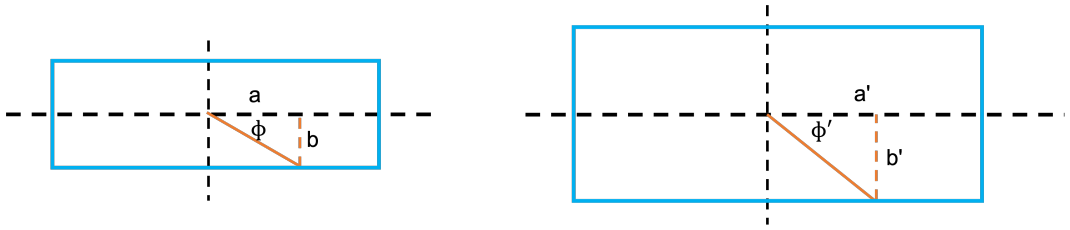

Fig. 3 Fibre re-orientation when subject to deformation.

$$\tan \phi_{i+1}^{(k)} = \frac{b_i}{a_i} = \frac{b(1+\varepsilon_{y,i}^{(k)})}{a(1+\varepsilon_{x,i}^{(k)})} = \tan \phi \frac{(1+\varepsilon_{y,i}^{(k)})}{(1+\varepsilon_{x,i}^{(k)})} \tag{10}$$

The residual is the given as the difference between the external force ($\mathbf{f}_{ext}(\mathbf{a})$) and internal force ($\mathbf{f}_{int}(\mathbf{a})$) vectors, as reported in Equation 11. From Equation 11 the residual stiffness matrix of the system can be computed as reported in Equation 12. The iterative process to determine the solution vector is reported in Equation 13. Here it can be seen that the solution vector updates each iteration with the dot product between the inverse of the stiffness matrix of the system at time step i ($\mathbf{K}_{sys,i}$) and the residual at time instance i ($\mathbf{r}_i$). This process is repeated until the residual is reduced to the desired value.

$$\mathbf{r}(\mathbf{a}) = \mathbf{f}_{ext}(\mathbf{a}) - \mathbf{f}_{int}(\mathbf{a}) \tag{11}$$

$$\mathbf{K}_{sys,i} = -\frac{\partial \mathbf{r}_i}{\partial \mathbf{a}} = \frac{\partial \mathbf{f}_{int}}{\partial \mathbf{a}} - \frac{\partial \mathbf{f}_{ext}}{\partial \mathbf{a}} \tag{12}$$

$$\Delta \mathbf{a}_{i+1} = \Delta \mathbf{a}_i + \mathbf{K}_{sys,i}^{-1} \mathbf{r}_i \tag{13}$$

The partial derivative of the internal force vector is the stiffness matrix of the vessel, as defined in Equation 6. The partial derivative of the external force vector, also known as the force stiffness matrix, is computed by differentiating the load vector as defined in Equation 6, with respect to the unknowns vector $\mathbf{a}$. The entries of the load vector are reported in Equation 28. The equations shows that the load vector entries have two components: material properties and layer radii. The material properties depend on the material itself, which does not change, and its orientation, which is said to change during the loading of the vessel. However, as the change in orientation is small, it is assumed that the change in material properties in the global coordinate system is negligible. The changes in radii are on the other hand taken into

account. This means that the derivative of the radius, and its powers, need to be computed. Starting from Equation 8, this leads to the relations reported in Equation 14.

$$\frac{\partial r_{i+1}}{\partial \mathbf{a}} = r_0 \frac{\partial \varepsilon_{\theta,i}}{\partial \mathbf{a}} \tag{14a}$$

$$\frac{\partial \left(r_{i+1}^2\right)}{\partial \mathbf{a}} = 2r_0^2 \left(1 + \varepsilon_{\theta,i}\right) \frac{\partial \varepsilon_{\theta,i}}{\partial \mathbf{a}} \tag{14b}$$

$$\frac{\partial \left(r_{i+1}^3\right)}{\partial \mathbf{a}} = 3r_0^3 \left(1 + \varepsilon_{\theta,i}\right)^2 \frac{\partial \varepsilon_{\theta,i}}{\partial \mathbf{a}} \tag{14c}$$

$$\tag{14d}$$

The derivative of the tangential strain in Equation 14 can be computed using the simplified strain relations and the assumed displacement field reported in Equation 1a, as depicted in Equation 15. Note that Equation 15 is for a single layer, with multiple layers, the vector is filled with zeros to account for the other $D^{(k)}$ and $E^{(k)}$ terms. Furthermore, the relation reports the derivative of the strain vector for the assumed deformation reported in Equation 1a, the same can be done for the assumed deformation reported in Equation 1b

$$\frac{\partial \varepsilon_\theta}{\partial \mathbf{a}} = \left[r^{\beta^{(k)}-1}, \quad r^{-\beta^{(k)}-1}, \quad \alpha_1^{(k)}, \quad \alpha_2^{(k)} r \right] \tag{15}$$

D. Buckling Analysis

Structures subjected to compressive loads can exhibit instability in the form of buckling. Hence it is essential to analyse both the inner and outer shells for potential compression-induced instabilities. The outer shell shall also be checked for external pressure buckling. The buckling loads of the composite shells are computed based on [7]. The buckling relations from [7] are reported in this section for completeness.

The buckling equation for axial compression is reported in Equation 16. Here the distributed buckling load (N_x) is given as a function of the cylinder length (L) and the A_{ij} terms, which can be determined using Equation 17. In Equation 17 the length and radius of the cylinder appear, with symbols L and r, respectively, and the properties of the laminate, which are included using the relations reported in Equation 18, Where the A_{ij}, B_{ij}, and D_{ij} terms are the entries of the ABD matrix of the laminate, to be obtained using classical laminate theory. Finally, the buckling load is a function of m and n, and as seen in Equation 17, these indicate the number of half waves of the buckled shape, which are to be altered with integer values to find the minimum load. The total buckling load is then obtained by multiplying the distributed buckling load by the perimeter of the cylinder.

$$N_x = \left(\frac{L}{m\pi}\right)^2 \frac{\begin{vmatrix} A_{11} & A_{12} & A_{13} \\ A_{21} & A_{22} & A_{23} \\ A_{31} & A_{32} & A_{33} \end{vmatrix}}{\begin{vmatrix} A_{11} & A_{12} \\ A_{21} & A_{22} \end{vmatrix}} \quad \text{for} \quad x \geq 4 \tag{16}$$

$$
\begin{aligned}
A_{11} &= \bar{E}_x \left(\frac{m\pi}{L}\right)^2 + \bar{G}_{xy} \left(\frac{n}{r}\right)^2 \\
A_{22} &= \bar{E}_y \left(\frac{n}{r}\right)^2 + \bar{G}_{xy} \left(\frac{m\pi}{L}\right)^2 \\
A_{33} &= \bar{D}_x \left(\frac{m\pi}{L}\right)^4 + \bar{D}_{xy} \left(\frac{m\pi}{L}\right)^2 \left(\frac{n}{r}\right)^2 + \bar{D}_y \left(\frac{n}{r}\right)^4 + \frac{\bar{E}_y}{r^2} + \frac{2\bar{C}_y}{r} \left(\frac{n}{r}\right)^2 + \frac{2\bar{C}_{xy}}{r} \left(\frac{m\pi}{L}\right)^2 \\
A_{12} &= A_{21} = \left(\bar{E}_{xy} + \bar{G}_{xy}\right) \frac{m\pi}{L} \frac{n}{r} \\
A_{23} &= A_{32} = \left(\bar{C}_{xy} + 2\bar{K}_{xy}\right) \left(\frac{m\pi}{L}\right)^2 \frac{n}{r} + \frac{\bar{E}_y}{r} \frac{n}{r} + \bar{C}_y \left(\frac{n}{r}\right)^3 \\
A_{31} &= A_{13} = \frac{\bar{E}_{xy}}{r} \frac{m\pi}{L} + \bar{C}_x \left(\frac{m\pi}{L}\right)^3 + \left(\bar{C}_{xy} + 2\bar{K}_{xy}\right) \frac{m\pi}{L} \left(\frac{n}{r}\right)^2
\end{aligned} \tag{17}
$$

$$
\begin{aligned}
\bar{E}_x &= A_{11} \qquad \bar{D}_x = D_{11} \quad \bar{C}_x = B_{11} \qquad \bar{G}_{xy} = A_{22} \\
\bar{E}_y &= A_{22} \qquad \bar{D}_y = D_{22} \quad \bar{C}_y = B_{22} \qquad \bar{K}_{xy} = B_{22} \\
\bar{E}_{xy} &= A_{12} \qquad \bar{D}_{xx} = D_{12} \quad \bar{C}_{xy} = B_{12}
\end{aligned} \tag{18}
$$

The equation for external pressure buckling is reported in Equation 19. The equation is given as a function of the terms as reported in Equation 17, the radius of the cylinder (r), and the number of halve waves (n), where the number of halve waves is determined by the minimum buckling load.

$$
N_x = \left(\frac{r}{n^2}\right)^2 \frac{\begin{vmatrix} A_{11} & A_{12} & A_{13} \\ A_{21} & A_{22} & A_{23} \\ A_{31} & A_{32} & A_{33} \end{vmatrix}}{\begin{vmatrix} A_{11} & A_{12} \\ A_{21} & A_{22} \end{vmatrix}} \tag{19}
$$

E. Manufacturing Considerations

The vessels are assumed to be manufactured using filament winding. As such, for each $+\phi$ layer, there shall be a $-\phi$ layer. These are assumed to be placed in blocks, leading to the following laminate type: $[\phi \backslash -\phi]_s$. The assumed laminate means that a minimum thickness needs to be included as a boundary condition, or a minimum number of layers, depending on how the optimisation is set up. In the current study, each layer is assumed to have a thickness of 0.125 mm, meaning that a minimum thickness of 0.5 mm is required.

During the non-linearisation of the analytical model described in subsection II.C, the variation of the angles in the lamination blocks are assumed to be constant, meaning that the change in rotation of the outer layers is equal to the change in rotation of the inner layers. The same goes for a change in thicknesses.

F. Optimisation Boundary Conditions

The Factor of Safety (FoS) can be computed with the non-linearised analytical model and the selected failure criterion. An FoS value smaller or equal to one indicates material failure. This value is shifted to zero, as is common when using optimisation algorithms. As such the non-linear inequality material failure boundary condition is set up as depicted in Equation 20.

$$
g_{material}(t, \phi) = FoS - 1 > 0 \tag{20}
$$

The axial buckling and vacuum buckling constraints are combined using the engineering approach. This means that the critical compression ratio and the critical pressure ratio are computed, as depicted in Equation 21. In the equation, p is the outer pressure on the vessel, which is assumed to be ambient pressure of 1 bar, while p_{cr} is the critical buckling pressure, computed with Equation 19. P in Equation 21 is the applied axial load to the cylinders, whereas P_{cr} is the critical axial buckling load obtained by multiplying the value obtained with Equation 16 with the perimeter of the cylinder.

$$R_p = \frac{p}{p_{cr}} \tag{21a}$$

$$R_c = \frac{P}{P_{cr}} \tag{21b}$$

$$\tag{21c}$$

The engineering approach states that failure occurs when the sum of the critical buckling ratios as derived in Equation 21 is greater or equal to one [7]. The suggested form is altered to perform better in an optimiser where values close to unity are desired. Due to the high non-linearity with respect to the thickness of the cylinder, it is chosen to take the logarithm of the sum of the ratios. The logarithm is multiplied by -1, such that positive values present the feasible domain. The non-linear inequality boundary condition for buckling becomes as depicted in Equation 22.

$$g_{buckle}(t, \phi) = -\log\left(R_p + R_c\right) > 0 \tag{22}$$

The minimal winding thickness, or minimum number of layers boundary condition, is included as a linear boundary condition, such that the minimum thickness of the lamination block as defined in subsection II.E is 0.5 mm, as depicted in Equation 23.

$$g_{thickness}(t, \phi) = t > 0.5 \tag{23}$$

III. Results

The goal of this study is to analyse which shell of a double-walled all-composite vacuum-insulated hydrogen storage vessel is more suited to carry an additional compressive load. This is done by studying how the boundary conditions described in the Methods section affect the design. subsection III.A studies how the viable design space changes for the inner shell housing the hydrogen, characterised by pressure and thermal loading. subsection III.B does the same for the outer shell, characterised by vacuum loading. subsection III.C summarises the results by visually determining the optimal solutions for the different loading conditions. Here it will be seen that, despite previously hypothesised, the inner shell is not necessarily more suited to carry the additional load. The outer shell, when accounting for other design considerations, may be more suited to carry compressive loads.

The results in this section are reported using contour plots, with an example reported in Figure 4a. The figures contain lines representing the material failure boundary condition in blue and the minimum thickness boundary condition reported in red. The buckling boundary condition, not present in Figure 4a, is presented in green. The continuous lines represent the positive viable side of the boundary condition, whereas the dashed lines represent the negative non-viable domain. On the y-axis, the variation in winding angle is found, whereas on the x-axis the variation in thickness is presented. This style of figure is consistent in the results section.

The inner and outer shells are studied with different loading cases. The inner shall has a base loading case of 500 bar. Additional loading cases are added to the base case, these include an increase in pressure, thermal loading, and axial loading. The base loading case is an eternal pressure of 1 bar. This loading case is then altered by adding the axial compressive load. The base dimensions of the shells is of 0.5 m and a length of 5.0 m. The dimensions of the outer shell are varied to study the effect the change in dimension has on the buckling boundary condition. An overview of the loading cases and the dimensions is reported in Table 2.

A. Inner Shell

In Figure 4a the shell has a radius of 0.5 m and is loaded with an internal pressure of 500 bar. The current case serves as a reference to analyse how the viable domain changes for varying loading conditions and dimensional changes. The minimum thickness boundary condition performs as expected, in a linear fashion dependent on the thickness of the vessel. The material failure boundary conditions behave as expected. Constant thickness lines resemble the ones found in literature [4]. Moreover, it can be seen that the thinnest vessel can be achieved at a winding angle slightly above 50°, which is in the proximity of the optimal winding angle of 54.74° [8].

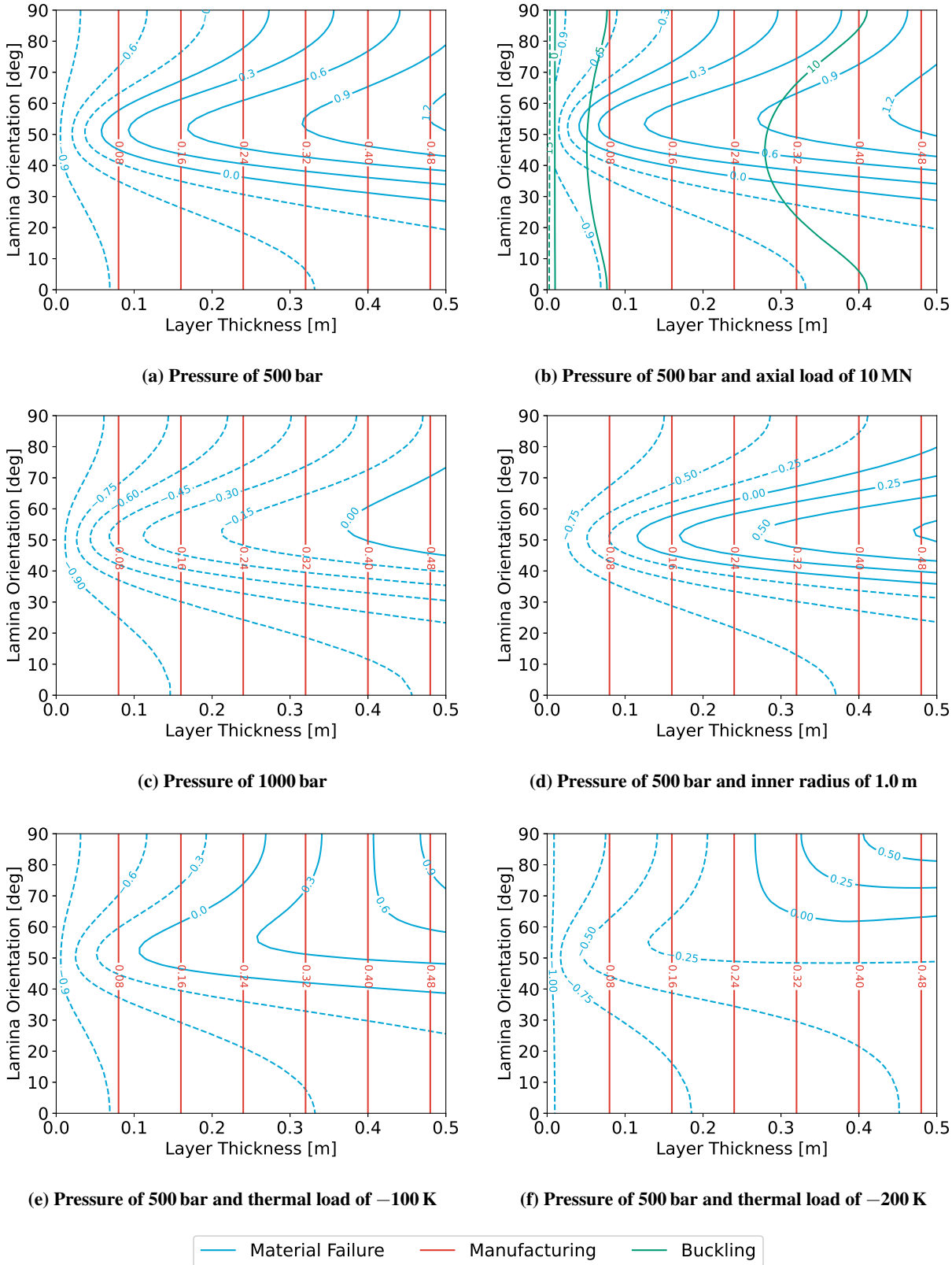

(a) Pressure of 500 bar

(b) Pressure of 500 bar and axial load of 10 MN

(c) Pressure of 1000 bar

(d) Pressure of 500 bar and inner radius of 1.0 m

(e) Pressure of 500 bar and thermal load of −100 K

(f) Pressure of 500 bar and thermal load of −200 K

Fig. 4 Material failure, minimal thickness, and buckling boundary conditions, for varying layer thickness and ply orientation for the outer shell for various load cases. Base radius is 0.5 m.

Figure 4b reports the boundary conditions for a composite shell loaded with an internal pressure of 500 bar and an axial compressive load of −10 MN. From the green buckling isoline of value 10, it can be seen that layers with 45° orientation are preferred, as is expected with buckling, where entries in the D matrix are of importance. The value of the buckling constraint highly depends on the thickness of the cylinder. The buckling boundary condition defines a minimum thickness for the vessel. The higher thickness defined by the material failure boundary condition renders this boundary inactive. The blue lines representing the material failure constraint display a similar trend to the one presented in Figure 4a. When studying the figure closely some differences can be found. First, the minimum thickness is lower. This is because the axial compressive load partially alleviates the extension loading in the axial direction of the vessel. The load alleviation in the axial direction means that fewer fibres are required in the longitudinal direction of the cylinder. As such the peak of the curve slightly shifts upwards to higher angle values.

Figure 4c depicts a similar contour plot, but for a vessel loaded with 1000 bar. The minimal thickness bounds are unchanged. The material failure bounds are shifted to the right-hand side, so higher thickness values are required to cope with the increased pressure value. A similar trend is observed in Figure 4d, where the vessel's radius is increased to 1.0 m. In thin-walled analysis, doubling the load or the radius leads to the same change in stress state [9]. When comparing Figure 4c and Figure 4d, it can be seen that this is not the case for thick-walled analysis. Here it is shown that the increase in pressure has much more effect on the stress state than the increase in radius, and thus on the viable domain.

In figures 4e and 4f, the vessels are loaded with a negative temperature delta of 100 K and 200 K, respectively, in addition to the inner pressure of 500 bar. In the figures, it can be seen that layups with low orientation angles become unviable. Based on netting analysis, tangential loading is twice the value of longitudinal loading. Traverse loading of longitudinally placed plies is further increased by the thermal contraction of the matrix in the traverse direction. It is deemed that the aforementioned phenomena render cylinders with low winding angles unviable.

Figure 5 presents the boundary conditions for a complete load case for the inner vessel, where the inner shell with radius 0.5 m is loaded with 500 bar, and axial compressive load of −10 MN, and a negative temperature delta of 200 K. The material failure contour lines are similar to the vessel loaded with a negative temperature gradient of 200 K presented in Figure 4f, with the lines slightly shifted to the left and a slight peak forms at winding angles around 60°. This can be explained by the material compression, assisting the contraction of the material, and favouring fibres in the axial loading direction. The figure also captures the minimum thickness objective. The full-colour area presents the viable domain, whereas the shaded domain presents the non-viable domain. The figure shows how the optimal thickness and winding angle can be located. In this case, it can be located with visual inspection in the small peak located at an angle value close to 60° with a thickness value close to 0.2 m, see Table 2 for more precise results.

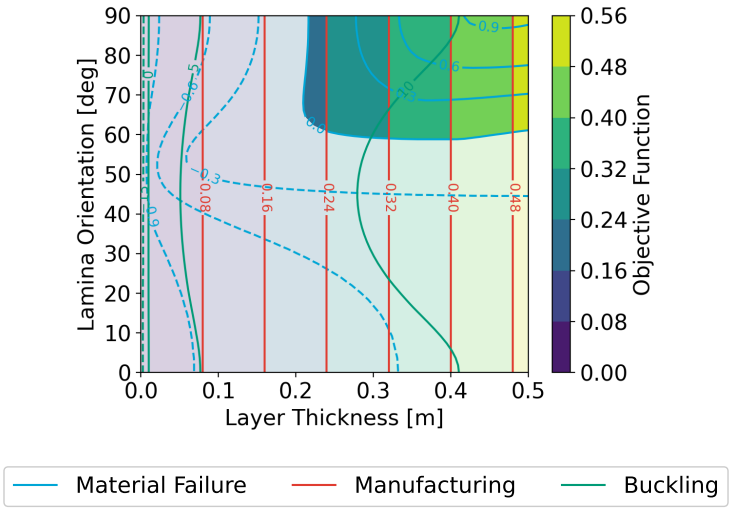

Fig. 5 Material failure, minimal thickness, and buckling boundary conditions, and minimal thickness objective, for varying layer thickness and ply orientation, for cylindrical shells with an inner radius of 0.5 m, loaded with 500 bar, an axial compressive load of −10 MN, and a negative temperature delta of 200 K

B. Outer Shell

Figure 6a presents the boundary conditions for the outer shell, which is loaded with an external pressure of 1 bar, has a length of 5.0 m and a radius of 0.5 m. Note that the outer composite shell results are reported using a different thickness scale on the x-axis with respect to the inner shell. The minimal thickness boundary condition remains unvaried, as the requirements are unchanged. The material failure boundary condition has high values, meaning that material failure is not the driving requirement for this composite shell. Instead, the buckling requirement is driving the design.

Figure 6b has an equal load case to the reference case, though the tank has its radius increased to 1.0 m. The material boundaries are affected by shifting to the right-hand side, though the values are still high. This is expected as an increase in radius leads to an increase in stress state. The buckling boundary conditions also become lower, making the structure more prone to buckling. A similar study has been done by doubling the vessel's length, though this has little influence on the buckling requirements, other than shifting the contour lines slightly to the left.

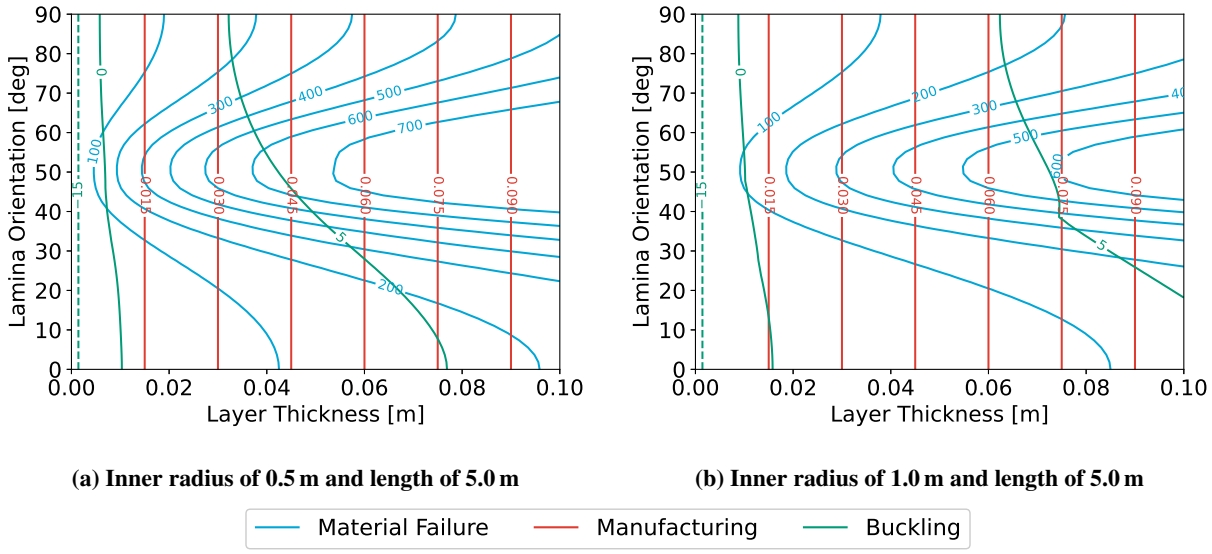

(a) Inner radius of 0.5 m and length of 5.0 m

(b) Inner radius of 1.0 m and length of 5.0 m

Fig. 6 Material failure, minimal thickness, and buckling boundary conditions, for varying layer thickness and ply orientation for vacuum loaded shell.

Figure 7 reports the contour lines where the external vacuum-loaded shell is subjected to an additional compressive load of -10 MN. The figure also reports the minimum thickness boundary objective, with the non-viable domain shaded in white. It can be seen that the material failure contour lines exhibit a different behaviour than before. It can be seen that layers with a null or 45° winding angle perform well. Other angles on the other hand perform badly, most likely because of the interaction between the two loading conditions, leading to compressive failure of the material. More research is required to investigate this behaviour further. In this case, the buckling boundary condition is similar to previously provided plots. It can be seen that for high winding angles the critical boundary transitions from being the buckling boundary condition to the material failure boundary condition, with the transition point laying around the winding angle value of 60°.

C. Shells Comparison

The current study aims to minimise the tank mass, as the fuel tank is intended for aviation applications. Therefore the optimal solution aims to minimise the thickness of the tank. Visually inspecting the presented charts, the optimal points have been determined, locating the left most viable point in the feasible domain. Table 2 presents a summary of the studied loading cases, where the optimal winding angle and thickness are extracted from the contour plots.

There are a few aspects that need to be addressed in the table. The e required thickness values for the thermally loaded tanks are excessively large. This would not be considered a viable design. As mentioned before, the thickness is driven by matrix failure. The temperature changes become more extensive should the tank undergo a thermal curing cycle during the manufacturing process. As alluded to before, an option could be to change the failure criterion to one

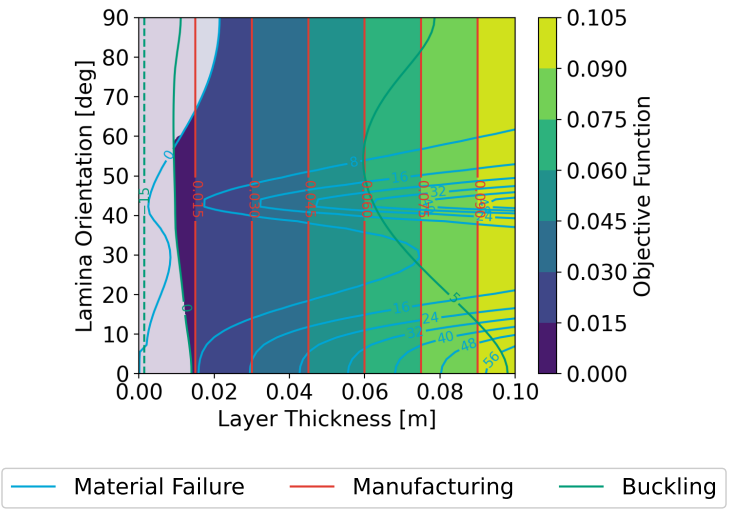

Fig. 7 Material failure, minimal thickness, and buckling boundary conditions, and minimal thickness objective, for varying layer thickness and ply orientation, for cylindrical shells loaded with an external pressure of 1 bar, and an axial compressive load of −10 MN.

Table 2 Optimal winding angle and thickness for different loading conditions of composite cylinders.

Tank shell	Length [m]	Radius [m]	Pressure [bar]	Axial Load [MN]	Thermal Loading [K]	Winding Angle [deg]	Thickness [mm]
Inner	5.0	0.5	500	0	0	51	58.1
Inner	5.0	0.5	1000	0	0	55	372.5
Inner	5.0	1.0	500	0	0	51	115.6
Inner	5.0	0.5	500	0	-100	52	106.6
Inner	5.0	0.5	500	0	-200	90	266.7
Inner	5.0	0.5	500	-10	0	53	41.1
Inner	5.0	0.5	500	-10	-200	68	209.6
Outer	5.0	0.5	-1	0	0	90	5.8
Outer	5.0	1.0	-1	0	0	90	8.9
Outer	10.0	0.5	-1	0	0	90	6.1
Outer	5.0	0.5	-1	-10	0	57	9.3

more suited for the given load case, such as one which only considers fibre failure. Implementing a different failure criterion affects other design choices for the hydrogen vessel. If matrix failure is accepted in the design, other problems may arise, such as leakage. This would necessitate the use of a liner. The material failure problem is further aggravated when the degradation of material properties is considered. The thermal load can be expected to decrease the ultimate failure load of the material, necessitating even larger thickness values, which is not realistic.

The winding angles also present some questionable results. Some charts show that the optimal design is characterised by a winding angle of 90°. An example is the vacuum-loaded outer shell, which fails in the buckling mode. From the buckling equations reported in 16 and 19, it is difficult to pinpoint which ABD matrix entries affect the buckling load. Nevertheless, an all-90 laminate is not considered viable [10]. This is a questionable design, as this would mean that there are no fibres in the longitudinal direction of the vessel. This behaviour subsides when the vessels are loaded with the additional axial load. In these cases, longitudinal fibres are required, lowering the optimal winding angle. A similar behaviour occurs when the inner shell is loaded thermally and axially. In future studies, it would be interesting to study

how this behaviour changes when multiple layers are enabled. Here one could also include boundary conditions which force the laminate to be more realistic, by including lamination requirements, such as the inclusion of 0, 90 and ±45 layers [10].

The difference in failure mode between the shells is also of importance. The outer shell tends to fail due to buckling, whereas the inner shell tends to fail due to material failure. The buckling failure mode is more desirable, as it is not necessarily a catastrophic failure, whereas material failure is. This naturally depends on what type of material failure is accepted. When looking at the results for the axially loaded shell, reported in Figure 7, the optimal solution lies at the intersection between the material failure and buckling boundary conditions. In this case study one could consider lowering the winding angle at the cost of a marginal thickness increase. By doing so, the material failure criterion becomes inactive, whereas the buckling condition becomes dominant, thus improving the safety of the design. Naturally, many other design considerations are to be accounted for. Nevertheless, this work provides valuable insight into how the failure modes interact and how this knowledge can be leveraged to achieve an efficient, yet safe design.

The goal of this work is to pinpoint which of the two composite shells is more suited to carry the additional external load. Despite the mentioned limitations, one can compare the effectiveness of the shells. The axial load partially alleviates the inner pressure load, enabling a smaller thickness, thus leading to a more lightweight structure. This however means that material failure occurs when the axial load is removed. This may be problematic as this is a realistic situation during operation. The outer shell's design, driven by the buckling boundary condition, is less sensitive to this behaviour. While the initial hypothesis suggested that the inner shell would be better suited to handle the additional load case, an alternative perspective arises, suggesting that the outer shell may, in fact, be more suitable for additional load-carrying duties.

IV. Conclusions and Recommendations

A method has been developed to define the viable design space for thick-walled all-composite cylinders, which are seen as part of a hydrogen storage vessel. The method enables the thermo-mechanical analysis of the structure, quantifying both material failure and instability failure. The method has been used to analyze a vacuum-insulated tank's inner and outer shells and determine which is better suited to carry an additional axial compressive load.

Some good results have been found, a few of which are outlined below:

- While in thin-walled analysis changes in pressure and radius lead to the same effect, when implementing thick-walled analysis it has been found that changing either of the two has a different effect on the loading of the vessel, and thus on the viable design space.
- Considering both matrix and fibre failure leads to non-viable designs when the vessel is loaded with a negative temperature difference. Which failure criterion is more suited for the studied load case should be investigated. Or it shall be investigated whether matrix failure can be accepted, by only considering fibre failure.
- The design of the inner shell is driven by material failure, whereas the outer shell is driven by geometric instability. The type of failure can be leveraged to achieve a failure mode which is more desirable. For example, by slightly changing the winding angle and thickness of the outer shell, the buckling failure mode can be made active, while deactivating the material failure mode.
- Adding axial loading to the inner shell enables thinner designs and an increase in winding angle, due to the decreased axial load. Removing the axial load would lead to the failure of the vessel. Adding the axial load to the outer shell has a small effect on the design of the vessel, and removing the load does not affect the failure of the vessel. As such the outer shell is deemed more viable to carry the axial compressive load.

Assumptions have been made that may require further investigation. When considering material failure, matrix failure is considered a failure of the vessel, which may not always be the case. A potential solution to this issue is only to consider fibre failure. Even better one could implement a failure criterion more suited for the thermo-mechanical loading case. Furthermore, material property degradation due to extreme thermal loading is not considered in the current study. The applied temperature load to the inner shell may be larger than the ones used in the current work, should the inner shell be subjected to a thermal curing cycle. On the other hand, no thermal load has been subjected to the outer shell, this may not be realistic as the vacuum vacuum between the shells is not necessarily a perfect insulator. The mentioned phenomena may be addressed in future work for a more realistic analysis.

Some obtained results require further investigation. The physical meaning of the shape of the contours representing material failure for the outer shell loaded in compression is unclear. A more thorough analysis of this is required to pinpoint the type of failure and how the winding angle influences this.

With some envisioned modifications, the value of the used model is further increased. For example, the model could be extended to account for additional loading conditions, as suggested in the Methods section. Currently, optimal winding angles and layer thicknesses have been found by visually inspecting the provided charts. The model can also be used to study a multi-layer tank, enabling different winding angles and thickness combinations. With the aid of an optimizer, the problem of increased degrees of freedom can be addressed. The computations are not expected to be expensive, as the constraints and objective functions are analytically determined.

With the current results and the envisioned future work, the authors aim to contribute to the development of hydrogen-powered aircraft, thereby supporting the aviation industry in its transition to a more sustainable future.

Appendix

$$d_1^{(k)} = r_k^{\beta(k)} \tag{24a}$$
$$d_2^{(k)} = r_k^{-\beta(k)} \tag{24b}$$
$$d_e^{(k)} = \alpha_1^{(k)} r_k \tag{24c}$$
$$d_t^{(k)} = \alpha_2^{(k)} r_k^2 \tag{24d}$$
$$\tag{24e}$$

$$s_1^{(k)} = (\bar{C}_{23}^{(k)} + \beta^{(k)} \bar{C}_{33}^{(k)}) r_k^{\beta(k)-1} \tag{25a}$$
$$s_2^{(k)} = (\bar{C}_{23}^{(k)} - \beta^{(k)} \bar{C}_{33}^{(k)}) r_k^{-\beta(k)-1} \tag{25b}$$
$$s_e^{(k)} = \bar{C}_{13}^{(k)} + \alpha_1^{(k)} (\bar{C}_{23}^{(k)} + \bar{C}_{33}^{(k)}) \tag{25c}$$
$$s_t^{(k)} = \left[\bar{C}_{36}^{(k)} + \alpha_2^{(k)} (\bar{C}_{23}^{(k)} + 2\bar{C}_{33}^{(k)}) \right] r_k \tag{25d}$$
$$\tag{25e}$$

$$e_1^{(k)} = \frac{\bar{C}_{12}^{(k)} + \beta^{(k)} \bar{C}_{13}^{(k)}}{1 + \beta^{(k)}} \left[r_{k+1}^{\beta(k)+1} - r_k^{\beta(k)+1} \right] \tag{26a}$$
$$e_2^{(k)} = \frac{\bar{C}_{12}^{(k)} - \beta^{(k)} \bar{C}_{13}^{(k)}}{1 - \beta^{(k)}} \left[r_{k+1}^{-\beta(k)+1} - r_k^{-\beta(k)+1} \right] \tag{26b}$$
$$e_e = \sum_{n=1}^{4} \left[\bar{C}_{11}^{(k)} + \alpha_1^{(k)} \left(\bar{C}_{12}^{(k)} + \bar{C}_{13}^{(k)} \right) \right] \frac{(r_{k+1}^2 - r_k^2)}{2} \tag{26c}$$
$$e_t = \sum_{n=1}^{4} \left[\bar{C}_{16}^{(k)} + \alpha_2^{(k)} \left(\bar{C}_{12}^{(k)} + 2\bar{C}_{13}^{(k)} \right) \right] \frac{(r_{k+1}^3 - r_k^3)}{3} \tag{26d}$$
$$\tag{26e}$$

$$t_1^{(k)} = \frac{\bar{C}_{26}^{(k)} + \beta^{(k)}\bar{C}_{36}^{(k)}}{2+\beta^{(k)}}\left[r_{k+1}^{\beta(k)+2} - r_k^{\beta(k)+2}\right] \tag{27a}$$

$$t_2^{(k)} = \frac{\bar{C}_{26}^{(k)} - \beta^{(k)}\bar{C}_{36}^{(k)}}{2-\beta^{(k)}}\left[r_{k+1}^{-\beta(k)+2} - r_k^{-\beta(k)+2}\right] \tag{27b}$$

$$t_e = \sum_{n=1}^{4}\left[\bar{C}_{16}^{(k)} + \alpha_1^{(k)}\left(\bar{C}_{26}^{(k)} + \bar{C}_{36}^{(k)}\right)\right]\frac{(r_{k+1}^3 - r_k^3)}{3} \tag{27c}$$

$$t_t = \sum_{n=1}^{4}\left[\bar{C}_{66}^{(k)} + \alpha_2^{(k)}\left(\bar{C}_{26}^{(k)} + 2\bar{C}_{36}^{(k)}\right)\right]\frac{(r_{k+1}^4 - r_k^4)}{4} \tag{27d}$$

(27e)

$$d_l^{(k)} = \frac{\eta^{(k)}}{1-\left(\beta^{(k)}\right)^2} r_{(k)} \tag{28a}$$

$$s_l^{(k)} = \frac{\eta^{(k)}}{1-\left(\beta^{(k)}\right)^2}\left[C_{33}^{(k)} + \bar{C}_{23}^{(k)}\right] - \xi_r^{(k)} \tag{28b}$$

$$e_l^{(k)} = \left[\frac{\eta^{(k)}}{1-\left(\beta^{(k)}\right)^2}\left[C_{13}^{(k)} + \bar{C}_{12}^{(k)}\right] - \xi_z^{(k)}\right]\left(r_{(k+1)}^2 - r_{(k)}^2\right) \tag{28c}$$

$$t_l^{(k)} = \frac{\eta^{(k)}}{1-\left(\beta^{(k)}\right)^2}\left[C_{26}^{(k)} + \bar{C}_{36}^{(k)}\right]\frac{\left(r_{(k+1)}^3 - r_{(k)}^3\right)}{3} \tag{28d}$$

(28e)

$$d_e^{(k)} = \alpha_3^{(k)}\frac{r_{(k)}\ln r_{(k)}}{2} \tag{29a}$$

$$s_e^{(k)} = \frac{\alpha_3^{(k)}\ln r_{(k)}\left(\bar{C}_{33}^{(k)} + \bar{C}_{23}^{(k)}\right) + \alpha_3^{(k)}\bar{C}_{33}^{(k)} + 2\bar{C}_{13}^{(k)}}{2} \tag{29b}$$

$$e_2^{(k)} = 2(\bar{C}_{12}^{(k)} - \bar{C}_{13}^{(k)})\ln\left(\frac{r_{(k+1)}}{r_{(k)}}\right) \tag{29c}$$

$$e_e^{(k)} = \alpha_3^{(k)}(\bar{C}_{13}^{(k)} + \bar{C}_{12}^{(k)})\left[\frac{r_{(k+1)}^2\ln r_{(k+1)} - r_{(k)}^2\ln r_{(k)}}{4} - \frac{r_{(k+1)}^2 - r_{(k)}^2}{8}\right] + \left(\frac{\alpha_3^{(k)}\bar{C}_{13}^{(k)}}{2} + \bar{C}_{11}^{(k)}\right)\frac{r_{(k+1)}^2 - r_{(k)}^2}{2} \tag{29d}$$

$$t_e^{(k)} = f(r_{(k+1)}) - f(r_{(k)}) \quad \text{where,} \quad f(r) = \left[\bar{C}_{16}^{(k)} - \frac{\alpha_3^{(k)}\bar{C}_{26}^{(k)}}{6} + \frac{\alpha_3^{(k)}\bar{C}_{36}^{(k)}}{3} + \frac{\alpha_3^{(k)}(\bar{C}_{26}^{(k)} + \bar{C}_{36}^{(k)})\ln r}{2}\right]\frac{r^3}{3} \tag{29e}$$

$$d_l^{(k)} = \eta^{(k)}\frac{r_{(k)}\ln r_{(k)}}{2} \tag{30a}$$

$$s_l^{(k)} = \frac{\eta^{(k)}\ln\left(r_{(k)}\right)\left[\bar{C}_{33}^{(k)} + \bar{C}_{23}^{(k)}\right] + \eta^{(k)}\bar{C}_{33}^{(k)}}{2} - \xi_r^{(k)} \tag{30b}$$

$$e_l^{(k)} = \eta^{(k)}(\bar{C}_{13}^{(k)} + \bar{C}_{12}^{(k)})\left[\frac{r_{(k+1)}^2\ln r_{(k+1)} - r_{(k)}^2\ln r_{(k)}}{4} - \frac{r_{(k+1)}^2 - r_{(k)}^2}{8}\right] + \left(\frac{\eta^{(k)}\bar{C}_{13}^{(k)}}{2} - \xi_z^{(k)}\right)\frac{r_{(k+1)}^2 - r_{(k)}^2}{2} \tag{30c}$$

$$t_l^{(k)} = f(r_{(k+1)}) - f(r_{(k)}) \quad \text{where,} \quad f(r) = \eta^{(k)}\frac{r^3}{6}\left[3\ln r\left(\bar{C}_{26}^{(k)} + \bar{C}_{36}^{(k)}\right) - \bar{C}_{26}^{(k)} + 2\bar{C}_{36}^{(k)} - 2\xi_{z\theta}^{(k)}\right] \tag{30d}$$

References

[1] Mital, S. K., Gyekenyesi, J. Z., Arnold, S. M., Sullivan, R. M., Manderscheid, J. M., and Murthy, P. L., "Review of Current State of the Art and Key Design Issues With Potential Solutions for Liquid Hydrogen Cryogenic Storage Tank Structures for Aircraft Applications," *NASA/TM-2006-214346*, 2006.

[2] Xia, M., Kemmochi, K., and Takayanagi, H., "Analysis of filament-wound fiber-reinforced sandwich pipe under combined internal pressure and thermomechanical loading," *Composite Structures*, Vol. 51, 2001, pp. 273–283. https://doi.org/10.1016/S0263-8223(00)00137-9.

[3] Xia, M., Takayanagi, H., and Kemmochi, K., "Analysis of multi-layered filament-wound composite pipes under internal pressure," *Composite Structures*, Vol. 53, 2001, pp. 483–491. https://doi.org/10.1016/S0263-8223(01)00061-7.

[4] Parnas, L., and Katırcı, N., "Design of fiber-reinforced composite pressure vessels under various loading conditions," *Composite Structures*, Vol. 58, No. 1, 2002, pp. 83–95. https://doi.org/10.1016/S0263-8223(02)00037-5.

[5] Evans, J. T., and Gibson, A. G., "Composite angle ply laminates and netting analysis," *Proceedings of the Royal Society A: Mathematical, Physical and Engineering Sciences*, Vol. 458, 2002, pp. 3079–3088. https://doi.org/10.1098/rspa.2002.1066.

[6] Dumanskii, A. M., Komarov, V. A., Alimov, M. A., and Radchenko, A. A., "On the effect of fiber rotation upon deformation of carbon-fiber angle-ply laminates," *Polymer Science - Series D*, Vol. 10, 2017, pp. 197–199. https://doi.org/10.1134/S199542121702006X.

[7] Hilburger, M. W., "Buckling of thin-walled circular cylinders," *NASA/SP-8007-2020/Rev 2*, 2020.

[8] Wild, P. M., and Vickers, G. W., "Analysis of filament-wound cylindrical shells under combined centrifugal, pressure and axial loading," *Composites Part A: Applied Science and Manufacturing*, Vol. 28, 1997, pp. 47–55. https://doi.org/10.1016/S1359-835X(96)00093-0.

[9] Tew, B. W., "Preliminary design of tubular composite structures using netting theory and composite degradation factors," *Journal of Pressure Vessel Technology, Transactions of the ASME*, Vol. 117, 1995, pp. 390–394. https://doi.org/10.1115/1.2842141.

[10] Kassapoglou, C., *Design and analysis of composite structures: With applications to aerospace structures*, John Wiley Sons, United States, 2010.